UC Irvine
UC Irvine Previously Published Works

Title
Scanning Laser Cavitation Rheology for mesoscopic mapping of shear moduli of soft materials at high strain rates

Permalink
https://escholarship.org/uc/item/52g8t5kz

Journal
Acta Biomaterialia, 214

ISSN
1742-7061

Authors
Sreedasyam, Rahul
Vu, Ethan C
Thota, Shreya
et al.

Publication Date
2026-04-01

DOI
10.1016/j.actbio.2026.03.024

Copyright Information
This work is made available under the terms of a Creative Commons Attribution License, available at https://creativecommons.org/licenses/by/4.0/

Peer reviewed

eScholarship.org Powered by the California Digital Library
University of California

Acta Biomaterialia 214 (2026) 392–402

Contents lists available at ScienceDirect

Acta Biomaterialia

journal homepage: www.elsevier.com/locate/actbio

Full length article

Scanning Laser Cavitation Rheology for mesoscopic mapping of shear moduli of soft materials at high strain rates

Rahul Sreedasyam [a], Ethan C. Vu [b], Shreya Thota [a], Elliot L. Botvinick [a,c,d,e,*], Vasan Venugopalan [a,b,c,f,*]

[a] Department of Biomedical Engineering, University of California Irvine, Irvine, CA 92697-2715, USA
[b] Department of Mechanical and Aerospace Engineering, University of California Irvine, Irvine, CA 92697-3975, USA
[c] Beckman Laser Institute and Medical Clinic, University of California Irvine, 1002 Health Sciences Road, Irvine, CA 92697-1475, USA
[d] Edwards Lifesciences Foundation Cardiovascular Innovation and Research Center, University of California Irvine, Irvine, CA 92697, USA
[e] Department of Surgery, University of California Irvine School of Medicine, Orange, CA 92868, USA
[f] Department of Chemical and Biomolecular Engineering, University of California Irvine, Irvine, CA 92697-2580, USA

ARTICLE INFO

Keywords:
High strain rate rheology
Laser-induced cavitation
Cavitation rheology
Mesoscale mechanical mapping
type-I collagen

ABSTRACT

Mechanical characterization of soft biomaterials is essential for understanding biological function, injury response, and the design of engineered tissues. Conventional techniques such as parallel-plate rheometry are restricted to bulk measurements at low to moderate mechanical strain rates ($< 10^2$ s^{-1}) and have limited relevance for the examination of high strain rate processes. We introduce scanning Laser Cavitation Rheology (sLCR) as a non-contact technique that utilizes single laser-generated microcavitation bubbles (μCBs) to map local shear modulus in soft hydrogels at strain rates exceeding 10^4 s^{-1}. Through a combination of probe beam measurement and single-frame shadowgraphy, we use a single pulsed laser exposure to measure the dynamics of μCB expansion and collapse to fit for shear modulus without high-speed videography, exogenous particles or repeated loading. We apply sLCR to type-I collagen (T1C) hydrogels and measure concentration-dependent shear moduli, establish relationships between local shear modulus and fiber architecture, and provide a practical framework for sLCR usage by defining sensitivity and spatial resolution limits. These results establish sLCR as a platform to provide localized, high strain rate measurements in biologically relevant 3D matrices, offering broad utility for mechanobiology, injury modeling, and mechanical characterization of complex soft biomaterials.

Statement of significance: Mechanical characterization tools typically resolve microscale properties at low strain rates or report bulk properties without spatial information. Scanning Laser Cavitation Rheology (sLCR) complements these methods by using single laser-generated microcavitation bubbles to measure mesoscale mechanical properties of soft biomaterials at high strain rates. We demonstrate the use of sLCR to measure concentration-dependent stiffening of type-I collagen, relate local elastic modulus to fiber architecture, and provide sensitivity and resolution limits. This method is compatible with commercial microscopy platforms, making it suitable for broad adoption. By enabling high strain rate, spatially resolved characterization of soft biomaterials, sLCR equips researchers to interrogate rapid loading events (e.g. blast injury, laser surgery) and chronic tissue remodeling (e.g. cancer, fibrosis).

1. Introduction

Mechanical characterization of soft biomaterials is essential for understanding how physical cues regulate cell behavior and disease. Foundational studies have established that extracellular matrix (ECM) mechanics can direct phenotype, lineage, and tumor progression [1–3]. More recently, local variations in ECM stiffness have been shown to influence stem cell differentiation, fibrosis, and cancer invasion [4,5]. However, conventional in vitro approaches for assessing ECM mechanics typically rely on bulk rheometry or inference based on hydrogel concentration [6,7]. While informative at the macro-scale, these methods overlook spatial heterogeneities in stiffness that arise from local variations in matrix structure and composition. Such heterogeneity is increasingly recognized as a critical regulator of mechanotransduction

* Corresponding authors.
E-mail addresses: ebotvini@uci.edu (E.L. Botvinick), vvenugop@uci.edu (V. Venugopalan).

https://doi.org/10.1016/j.actbio.2026.03.024
Received 3 November 2025; Received in revised form 5 March 2026; Accepted 10 March 2026
Available online 11 March 2026
1742-7061/© 2026 The Authors. Published by Elsevier Inc. on behalf of Acta Materialia Inc. This is an open access article under the CC BY-NC-ND license (http://creativecommons.org/licenses/by-nc-nd/4.0/).

in health and disease [8,9].

The development of micro- and mesoscale techniques such as optical coherence elastography [10], laser speckle rheology [11], and optical tweezers microrheology [12–14] have provided new avenues to bridge this resolution gap, enabling local measurements of ECM stiffness in the quasi-static and low strain rate regimes (Fig. 1). However, many clinically relevant events such as traumatic brain injury (TBI) [15,16], laser surgery [17,18], and shock-wave lithotripsy [19] expose tissues to large mechanical strains ($>10^{-1}$) and strain rates ($>10^4$ s^{-1}). At present, few experimental methods exist to interrogate soft material mechanics under these conditions. The Split-Hopkinson (Kolsky) pressure bar remains the gold standard for high strain rate mechanical testing, but its reliance on stress wave propagation makes it poorly suited for spatially heterogeneous, low-wave speed biomaterials [20].

Cavitation-based rheology has emerged as a promising approach for mechanical characterization of soft materials at high strain rates, encompassing needle-induced cavitation rheology [21], laser-induced membrane expansion [22], acoustic cavitation rheology [23], and laser-induced microcavitation approaches [24–26]. By generating laser-induced cavitation bubbles, measuring their oscillatory dynamics, and fitting these measurements to a theoretical model, it is possible to estimate the surrounding material's mechanical properties [24]. While cavitation rheology represents a major advancement in the field, existing implementations are primarily designed to extract material properties at a single location by fitting the full bubble dynamics $R(t)$, often using expensive and specialized ultra-high-speed videography hardware [24]. By contrast, there remains a need for a cavitation rheology method that enables spatially resolved measurements of high strain rate material properties on the mesoscopic scale, using instrumentation that is practical for broad adoption by biomaterials and mechanobiology laboratories. Existing approaches also face several important limitations, including the use of exogenous probes or light-absorbing particles [21,26], need for multiple cavitation events to obtain a single measurement [25], and incompatibility with co-registered imaging modalities such as laser scanning confocal microscopy. Such constraints have impeded the broad adoption of cavitation rheology as a practical tool for mechanical mapping of soft biomaterials.

Here, we introduce scanning Laser Cavitation Rheology (sLCR) as a probe-free, non-contact method that utilizes cavitation rheology for spatial mapping of high strain rate shear modulus (G_{HSR}) in soft biomaterials. By combining the generation of single, ~200 μm diameter laser-induced microcavitation bubbles (μCBs) in a raster pattern with measurement and analysis of their dynamics, we demonstrate that sLCR obtains spatially resolved measurements of local G_{HSR} with submillimeter, mesoscale (~300 μm) resolution at strain rates exceeding 10^4 s^{-1}. Unlike prior implementations of cavitation rheology, sLCR does not require high-speed videography or exogenous absorbers. Moreover, sLCR requires only a single cavitation event per measurement, and can be implemented on a commercial laser scanning microscope. We demonstrate the utility of sLCR in hydrogels composed of type I collagen (T1C), a widely used model ECM due to its abundance in native tissue [27,28]. In this study, we use sLCR to capture T1C concentration-dependent trends in G_{HSR}, reveal the structural basis of stiffening via co-registered reflection confocal imaging, and define the technique's sensitivity and spatial resolution limits.

2. Materials and methods

2.1. Experimental setup

Single microcavitation bubbles (μCBs) were generated by introducing the emission from a frequency-doubled Nd:YAG picosecond laser (EKSPLA PL2210, λ=532 nm) providing single 24 ps pulses into the left side port of a laser scanning confocal microscope (Evident IX83 FV3000) (Fig. 2A). The laser beam was collimated and directed into the rear aperture of a 10× microscope objective (NA=0.4, Evident UPlanXApo10X). To minimize boundary effects, the focal volume of the pulsed laser beam was positioned near the center of the dish (lateral clearance $> 10R_{max}$) and at a depth of 300 μm ($> 2.5R_{max}$) above the coverslip of a glass-bottom petri dish (World Precision Instruments FD35). We utilized a fixed laser pulse energy of 0.77 μJ, verified via measurement at the rear aperture of the objective using an energy meter (MKS Newport 843-R). These pulses produced μCBs of a consistent size within the hydrogels with maximum radii in the range of 100–125 μm, depending on the

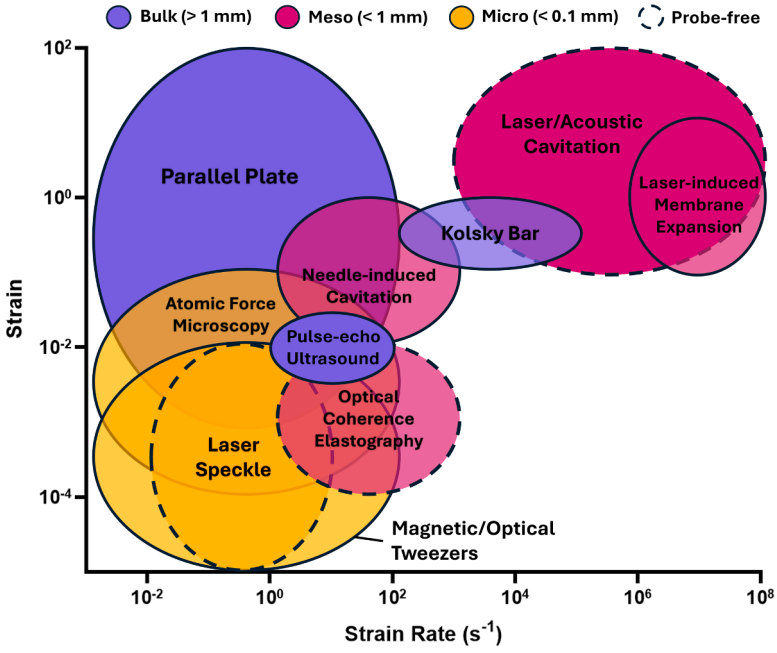


Fig. 1. Regimes of applied strain and strain rate accessed by current mechanical characterization methods. Methods are categorized by their effective spatial scale: bulk (>1 mm, purple), mesoscale (<1 mm, pink), and microscale (<0.1 mm, yellow). Techniques enclosed by dashed outlines indicate probe-free approaches. Laser-induced cavitation rheology occupies a previously underexplored regime of high strain and high strain rate, enabling probe-free mechanical interrogation at submillimeter spatial scales. These regimes are approximate and may vary based on the specific implementation and experimental conditions.

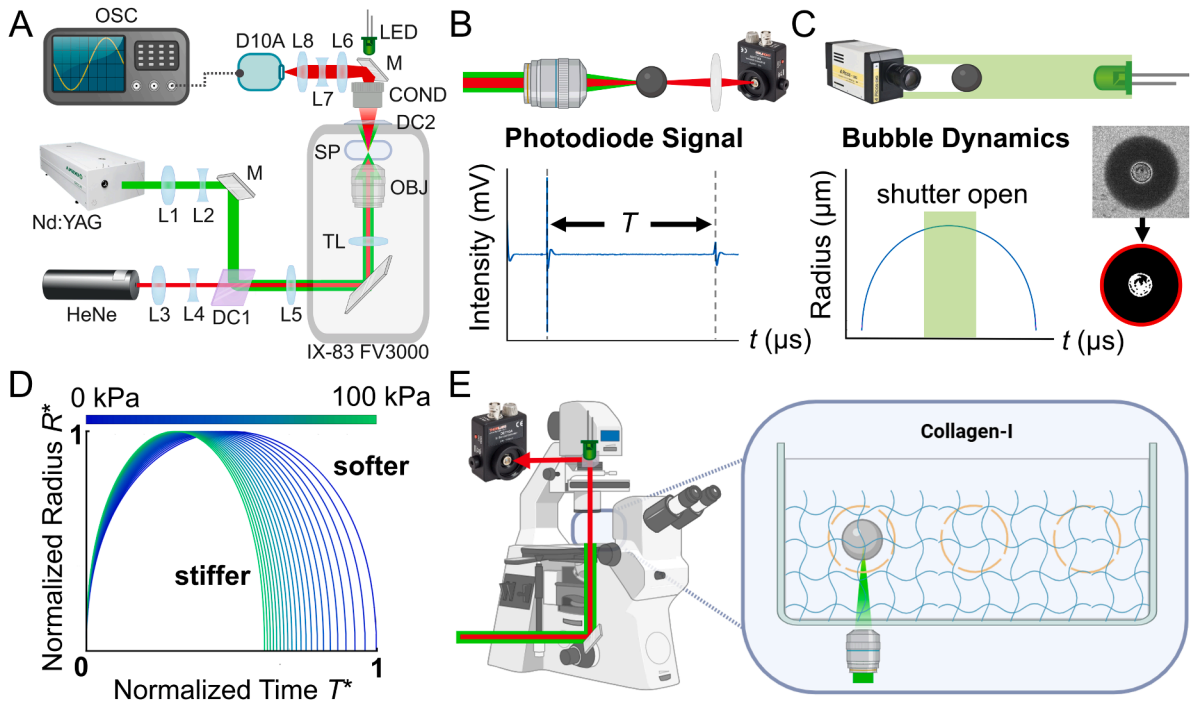


Fig. 2. Overview of the scanning Laser Cavitation Rheology (sLCR) apparatus. (A) Optical layout for sLCR. The gray shaded region represents the laser scanning confocal microscope used for μCB generation and co-registered imaging. (B) Measurement of μCB oscillation time using the laser probe beam and photodiode in the sLCR apparatus. The sharp peaks in photodiode signal intensity correspond to μCB initiation and end of μCB collapse. (C) Shadowgraph setup used to capture the maximum μCB radius, with an ICCD camera shutter synchronized to the laser pulse. The red outline indicates computed maximum radius. (D) Effect of shear modulus on normalized bubble dynamics simulated using a Neo-Hookean bubble model, plotted as normalized radius $R^* = R/R_{max}$ as a function of normalized time $T^* = (T/1.83R_{max})(p_\infty/\rho)^{1/2}$. (E) Schematic of the experimental design showing an array of sLCR measurements within a T1C hydrogel.

collagen concentration. In deionized (DI) water, this pulse energy yielded consistent maximum μCB radii of approximately 105 μm (Supplementary Fig. S1).

2.2. Laser probe beam measurement of μCB oscillation time

To monitor μCB oscillation time, a continuous wave 12 mW HeNe laser (λ = 632.8 nm, Newport Optics R-30993) beam was co-aligned with the pulsed Nd:YAG laser used for cavitation bubble generation. The HeNe laser served as a probe beam and illuminated the sample only when the microscope turret was opened to deliver the Nd:YAG laser pulse (<4 s per site). The μCB formation, growth, and collapse alter the transmission efficiency of the HeNe laser probe beam and was detected as a modulation of its transmitted intensity using a silicon photodiode (Thorlabs DET10A; 150 MHz bandwidth; 1 ns rise time) placed behind the microscope condenser lens and digitized at 10 GS/s on an oscilloscope (LeCroy WaveRunner 6200A; 2 GHz). The oscilloscope was triggered by the Nd:YAG pulse laser (EKSPLA PL2210; <10 ps jitter). Altogether, this system provided overall timing precision of ~2 ns. Each μCB produced sharp peaks in probe beam intensity, corresponding to bubble formation, end of the first bubble collapse, and subsequent rebounds; thereby providing a quantitative measurement of the μCB oscillation time (Fig. 2B). Photodiode signals were analyzed using a custom MATLAB script. This script utilizes the `findpeaks` command to automatically detect the intensity peak corresponding to bubble initiation and the subsequent peak corresponding to the end of the first bubble collapse. The time interval between these two peaks was defined as the μCB oscillation time.

2.3. High-speed shadowgraph measurement of maximum μCB radius

The maximum radius R_{max} of each μCB was measured via high-speed shadowgraphy using an intensified charge-coupled device (ICCD) camera (4-Picos, Stanford Computer Optics). A 3 W, 532 nm light emitting diode (LED) light source (CHANZON) was positioned beneath the microscope condenser, replacing the standard transmission lamp to provide uniform illumination during image acquisition. A 600 nm short-pass filter was placed in front of the camera to block light from the HeNe probe beam. For each T1C hydrogel concentration measured, we first produced μCBs in a separate T1C hydrogel target and acquired images using a range of ICCD delay times (1–25 μs) to locate the time of maximum radius $t(R_{max})$ and found that across all concentrations tested, $t(R_{max})$ occurred within 7–13 μs following μCB initiation. This is consistent with theoretical predictions from the modified Rayleigh-Plesset equation for viscoelastic materials described by Gaudron et al. [29] (Supplementary Fig. S2). Accordingly, the ICCD camera shutter was programmed to open for a 6 μs duration with a 7 μs delay. This timing ensures that the shutter is open after delivery of the Nd:YAG laser pulse but during the time of maximum bubble expansion for all hydrogel concentrations tested. As the μCB expands and collapses, it transiently obstructs the LED emission from reaching the camera sensor, casting a dark circular shadow whose radius corresponds to that of the μCB (Fig. 2C). Captured images were analyzed using a custom MATLAB script. The `imfindcircles` command was used to automatically segment the shadowgraph and extract the R_{max} value via a circular Hough transform.

2.4. Modeling μCB dynamics

The μCB dynamics were modeled using a modified Rayleigh-Plesset equation (RPE) described by Gaudron et al. [29], which describes bubble dynamics in a Neo-Hookean medium with the assumption of negligible material compressibility. The governing equation is:

$$R_B\frac{d^2R_B}{dt^2}+\frac{3}{2}\left(\frac{dR_B}{dt}\right)^2=\frac{p_B-p_\infty}{\rho}-\frac{2S}{\rho R_B}-\frac{4\nu}{R_B}\frac{dR_B}{dt}-\frac{\sigma}{\rho} \quad (1)$$

where R_B is the instantaneous bubble radius that evolves with time t, ρ is the material density, ν is the kinematic viscosity of the interstitial fluid, S is the surface tension at the bubble surface, p_B is the internal bubble pressure, p_∞ is the far-field ambient pressure, and σ is the elastic stress that the material imposes onto the bubble. In this framework, ρ, ν, and S correspond to the properties of the interstitial aqueous phase of the hydrogel. For type-I collagen gels prepared in PBS, we use values for DI water at 25 °C, which differ minimally from those of PBS [30–32]. Users working with different interstitial media should substitute appropriate values.

The elastic stress term σ is derived from a Neo-Hookean model and is expressed as:

$$\sigma = \frac{G_{HSR}}{2}\left[5 - 4\left(\frac{R_0}{R_B}\right) - \left(\frac{R_0}{R_B}\right)^4\right] \quad (2)$$

Where G_{HSR} is the effective high strain rate shear modulus of the surrounding material and R_0 is the equilibrium bubble radius.

Here, the equilibrium bubble radius R_0 denotes the size of the cavity before stress is applied to the external material. In our experiments, R_0 is not directly imaged. Our methodology utilizes the acquisition of only a single image, which we use to capture the maximum bubble size R_{max}. Consistent with prior cavitation rheology studies [25,33], we assume the bubble interior is vapor-dominated at maximum expansion, such that the internal bubble pressure p_B at R_{max} is equivalent to the vapor pressure p_v, and that it evolves adiabatically over the first μCB oscillation. Accordingly, we model the internal bubble pressure as:

$$p_B(R_B) = p_v{}^*\left(\frac{R_{max}}{R_B}\right)^{3\kappa} \quad (3)$$

where p_v is the vapor pressure within the bubble (3170 Pa for water at 25 °C) and κ is the adiabatic index. The corresponding equilibrium bubble radius R_0 is obtained by setting $p_B(R_0) = p_\infty$, giving:

$$R_0 = R_{max}\left(\frac{p_v}{p_\infty}\right)^{\frac{1}{3\kappa}} \quad (4)$$

For the R_{max} range employed here (100–125 μm), this yields R_0 values ranging from ~40–50 μm in both collagen gels and DI water; approximately an order of magnitude larger than the characteristic pore size of T1C hydrogels [34].

We also assume thermal and mass transfer effects to be negligible because our approach relies only on the first μCB oscillation (~20 μs), during which time such effects have a negligible effect on the collapse time [35]. Moreover, given our simplified approach, we cannot independently fit for G_{HSR} and a viscous parameter without using an empirically calibrated relationship between shear modulus G and material viscosity μ [36] or obtaining additional data regarding the μCB dynamics [37]. Consequently, we do not claim an independent estimation of both G_{HSR} and viscosity from oscillation time alone. Instead, our implementation yields G_{HSR} under the assumed interstitial fluid viscosity.

2.5. Determination of local high strain rate shear modulus

The shear modulus G_{HSR} within a T1C hydrogel was obtained by forward simulation of the bubble dynamics model using the experimentally measured maximum μCB radius as an initial condition. For a given bubble size, softer materials yield longer oscillation times (Fig. 2D). A range of candidate G_{HSR} values were tested, and the value that minimized the difference between the simulated and experimentally measured oscillation time was selected. This one-parameter inverse problem was solved using a bounded search algorithm implemented in MATLAB. A depiction of the sLCR workflow and analysis is shown in Fig. 3.

μCB measurements were first performed in deionized (DI) water, in which the expected G_{HSR} is zero. The modeling parameters ρ (material density), ν (kinematic viscosity), S (surface tension), and p_v (vapor pressure) under these conditions were used as a baseline to confirm that the modeling framework does not artificially detect an elastic response in a purely Newtonian fluid. These baseline parameters were then held constant for all subsequent hydrogel simulations, such that G_{HSR} was the only adjustable parameter used to fit the data.

2.6. Spatial mapping of shear modulus

To generate spatial maps of shear modulus G_{HSR}, μCBs were generated at defined positions across the sample by translating the stage in a raster pattern with 318.2 μm spacing. Measurements were conducted in a 4 × 4 grid pattern spanning a 1.27 × 1.27 mm^2 region for a total of 16 measurements per hydrogel sample. At each position, a single μCB was generated, measured, and processed to extract G_{HSR} (Fig. 3). Colormaps representing the magnitude of G_{HSR} were constructed by assembling the shear modulus values into a 2D grid using the `heatmap` function in MATLAB. Measurements were excluded from analysis if the μCB shadowgraph was not detected as a circle by the circular Hough transform (MATLAB `imfindcircles`). The proportion of invalid measurements was 4.1 % for the 1.0, 1.5, and 2.0 mg/mL gels, and 8.2 % for the 2.5 mg/mL condition (n = 48 measurements per condition). All invalid measurements were excluded from subsequent analyses.

To visualize the hydrogel microstructure, reflection confocal microscopy (λ = 488 nm) was performed using a 40× silicone oil microscope objective (NA=1.25, Evident UPlanSApo40X), before each μCB exposure. The imaging parameters used in this study resulted in a 318.2

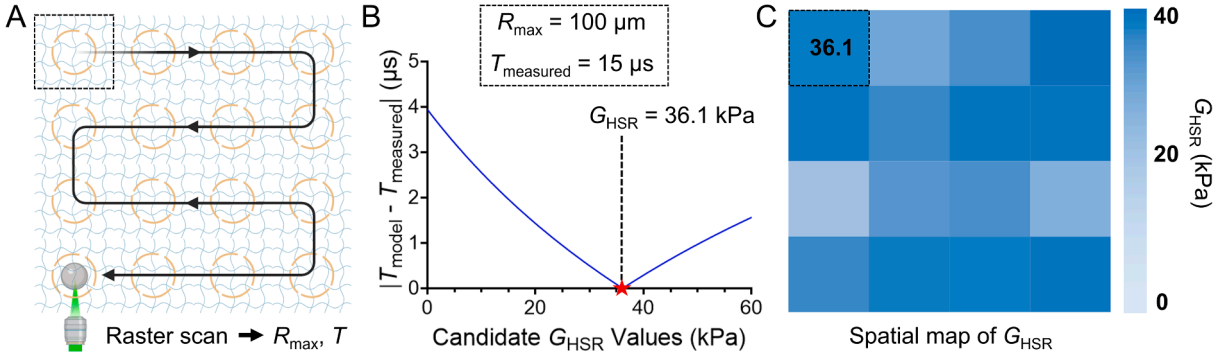


Fig. 3. sLCR workflow and analysis. (A) μCBs are generated in a raster pattern across the hydrogel, yielding measurements of maximum R_{max} and oscillation time T. (B) Representative estimation of G_{HSR} (dashed box): for the measured R_{max}, the forward model is evaluated over candidate G_{HSR} values and the inferred modulus is selected by minimizing T_{model}-$T_{measured}$ (red star). (C) Repeating this procedure for the cavitation bubble generation at each raster site provides a spatial map of G_{HSR} (color scale).

× 318.2 μm^2 optical section located 300 μm above the coverslip of a glass-bottom petri dish. Immediately following image capture, the automated filter cube turret of the microscope switched from a silver mirror to an empty position, and the automated objective turret switched to the 10× objective to permit delivery of a single laser pulse into the sample to generate a μCB. The maximum μCB radius R_{max} and oscillation time T were automatically determined as described above and illustrated in Fig. 2B-C. Following μCB generation, both turrets returned to the image acquisition configuration, and the stage was moved to the next location. Raster scanning of μCBs in a grid pattern was automated using the multi-area time lapse (MATL) feature of the microscope.

2.7. Hydrogel preparation

Type 1 acetic acid-extracted rat tail collagen (Advanced Biomatrix, #5153) hydrogels were prepared at concentrations of 1.0, 1.5, 2.0, and 2.5 mg/mL following the manufacturer's protocol. This T1C was neutralized on ice using the supplied neutralization solution and diluted to the desired concentration with 10x PBS supplemented with 10 mM HEPES to buffer pH. Each sample consisted of a total volume of 666 μL plated onto a 35 mm diameter glass-bottom dish and incubated at 37 °C for 60 min for polymerization to occur, followed by rehydration with 10x PBS (Gibco). The final hydrogel was approximately 1 mm thick. Air bubble formation was minimized via careful mixing and handling during preparation. All experiments were performed 24 h after gel polymerization.

2.8. Bulk rheometry

To provide benchmark values for the conventional shear modulus at low strain and strain rates, we performed bulk rheology on our T1C samples using a rotational parallel-plate rheometer (Anton Paar, MCR-301). Non-polymerized collagen solutions were loaded directly onto the lower parallel plate, and the upper plate was lowered quickly to a 0.2 mm gap distance, allowing the sample to polymerize between the parallel plates at 37 °C. Samples were not trimmed after loading to preserve their mechanical integrity, and a solvent trap was used to prevent evaporation. All measurements were conducted using a 25 mm diameter parallel plate during polymerization at 37 °C, with a frequency of 1 Hz and strain amplitude of 1 % (Supplementary Fig. S3).

2.9. Fiber structure analysis

Collagen fiber structure was assessed using GTFiber, an open-source software package for automated segmentation and analysis of fibrillar networks [38,39]. Reflection confocal images of T1C hydrogels were first pre-processed by applying a black circular mask to exclude the central reflection artifact, ensuring accurate fiber detection. The processed images were then analyzed in GTFiber to generate vector maps of collagen fibers and compute mean fiber length, mean fiber width, and fiber length density within a 318.2 × 318.2 μm^2 region of interest. Fiber length density was defined as the total length of fibers per unit area, expressed as μm^{-1}. The segmentation parameters used for this analysis are shown in Supplementary Fig. S4.

2.10. Statistical methods

Statistical analyses were conducted using GraphPad Prism. Data are reported as mean ± standard deviation, unless otherwise specified. For all experiments, $n \geq 3$ independent hydrogel samples were tested for each condition. Normality was assessed using the Shapiro-Wilk test and all data were found to deviate from normality ($p < 0.05$). Therefore, group comparisons across collagen concentrations were assessed using the nonparametric Kruskal-Wallis test followed by Dunn's multiple comparisons test. Correlations between G_{HSR} and fiber metrics were analyzed using Spearman's rank correlation coefficient r, with associated p-values reported to assess significance. Statistical significance was defined as $p < 0.05$.

3. Results

3.1. Effect of T1C concentration on high strain rate shear modulus

sLCR was applied to T1C hydrogels formulated at concentrations of 1.0, 1.5, 2.0, and 2.5 mg/mL. Both the maximum μCB radius R_{max} and the oscillation time T decreased monotonically with increasing collagen concentration (Fig. 4A-B). These trends correspond to an increase in shear modulus G_{HSR} (Fig. 4C), indicating stronger resistance to cavitation-induced deformation in denser collagen matrices. All pairwise differences in R_{max}, T, and G_{HSR} were statistically significant ($p < 0.05$). Our analysis revealed that G_{HSR} increased with collagen concentration as follows: 11.4 ± 2.3 kPa (@1.0 mg/mL), 17.3 ± 2.3 kPa (@1.5 mg/mL), 24.5 ± 2.8 kPa (@2.0 mg/mL), and 28.5 ± 3.0 kPa (@2.5 mg/mL). Replicate gels at each concentration ($n = 3$) exhibited no statistically significant differences in G_{HSR} (Supplementary Fig. S5).

3.2. Spatial mapping of high strain rate shear modulus in T1C hydrogels

To assess local mechanical properties of collagen hydrogels, sLCR was used to generate μCBs in a raster-scanning pattern within collagen hydrogels. Spatial maps of shear modulus G_{HSR} were produced for each sample, with representative maps from 1.0, 1.5, 2.0, and 2.5 mg/mL collagen shown in Fig. 5A. Replicate maps for each concentration are shown in Supplementary Figs. S6–9. These maps illustrate the distribution of G_{HSR} values obtained across a sample. Co-registered reflection confocal images were acquired at each μCB location and displayed below each shear modulus colormap (Fig. 5B), enabling direct comparison of local G_{HSR} measurements with microstructural features of the hydrogel.

3.3. Shear modulus is correlated with collagen fiber properties

To explore the structural determinants of local mechanical properties, we analyzed the fiber network at each sLCR measurement location using the open-source software package GTFiber [38,39]. As shown in Fig. 6, increasing T1C concentration resulted in a monotonic decrease in mean fiber length and increases in both the mean fiber width and fiber length density (Fig. 6A-C). When data were pooled across all T1C concentrations, the local shear modulus G_{HSR} exhibited significant correlations ($p < 0.0001$) with fiber length, width, and length density (Fig. 6D-F). Notably, we observed substantial variability in these fiber metrics within each concentration, consistent with mesoscale microstructural variability in nominally "homogeneous" gels. For a given hydrogel concentration, no significant correlations with G_{HSR} were observed ($p \gg 0.05$), suggesting that the variation in G_{HSR} across samples within a single concentration is not captured by any single fiber metric quantified here. The absence of significant differences in G_{HSR} across replicate gels of a single concentration (Supplementary Fig. S5) indicates that the observed variability occurs within individual gels rather than between replicate gels.

3.4. Cavitation-induced damage defines the spatial resolution limit of sLCR

We hypothesized that μCB-induced matrix damage (Fig. 7A) would locally soften the surrounding region, thereby influencing subsequent measurements and effectively limiting the spatial resolution of the technique. To test this, laser pulses were delivered at center-to-center distances of 53, 160, 266, and 373 μm, corresponding to approximately 0.5×, 1.5×, 2.4×, and 3.4× R_{max}, respectively (Fig. 7B). Contrary to our hypothesis, we observed an apparent "stiffening" effect

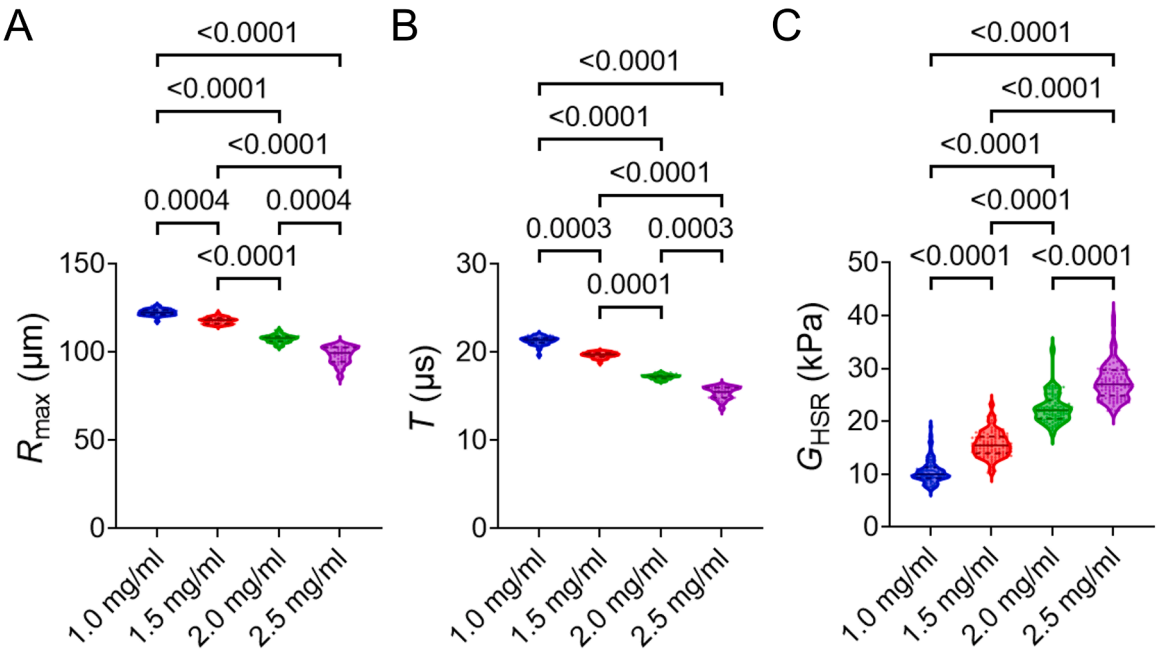


Fig. 4. Effect of T1C concentration on (A) maximum μCB radius R_{max}, (B) μCB oscillation time T and (C) shear modulus G_{HSR} measured by sLCR. Statistical comparisons were performed using the Kruskal-Wallis test with Dunn's multiple comparisons. Data represent $n = 48$ measurements per condition across 3 independent hydrogel samples.

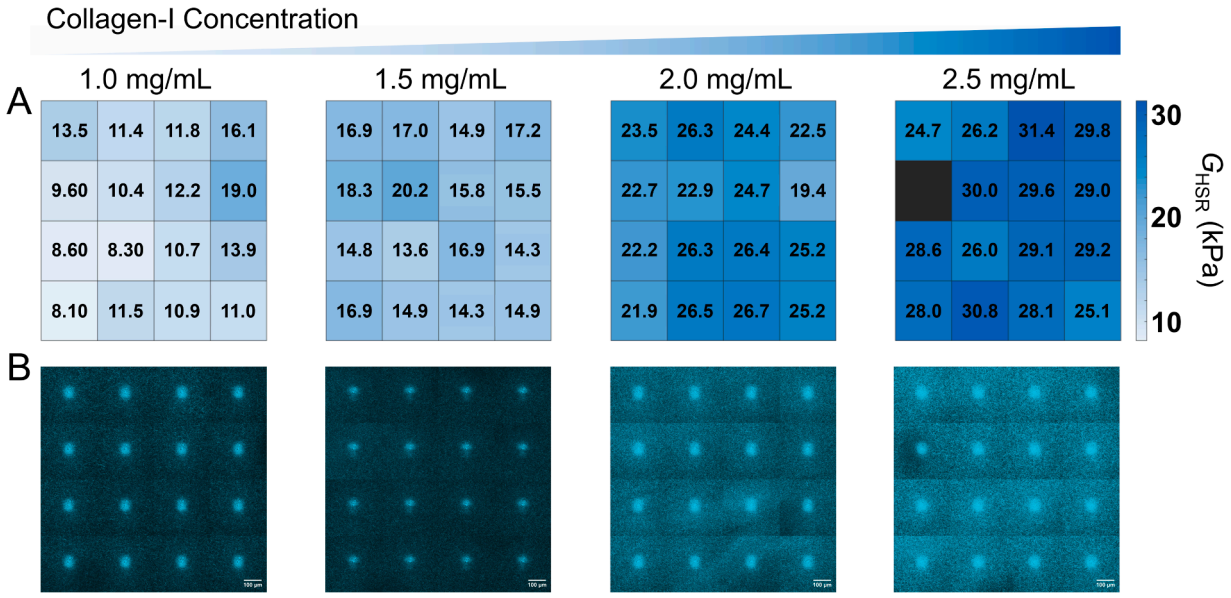


Fig. 5. Mapping of G_{HSR} and spatially co-registered imaging of T1C hydrogels. (A) Representative spatial maps reveal measurements of shear modulus G_{HSR}. Values are reported in kPa. Dark squares represent invalid measurements excluded from analysis. (B) Co-registered reflection confocal microscopy images (Evident UPlanSApo40X, 1.25 NA) showing collagen fiber architecture at measurement sites across a 4 × 4 measurement grid. Bright spots indicate diffraction rings characteristic of reflection confocal images. Scale bar = 100 μm.

when the second μCB was generated at all locations within approximately 2.5 maximum μCB radii of a previous μCB site (Fig. 7C). Specifically, while the second μCB had a larger maximum radius, typically indicative of material softening, a corresponding increase in oscillation time was not observed. This resulted in a misleading inference of an elevated shear modulus G_{HSR} (Supplementary Fig. S10). This effect was more pronounced in higher concentration T1C hydrogels.

Closer inspection of the laser probe beam signal when the second μCB was generated at a distance $<2.5R_{max}$ revealed the absence of the characteristic features of a rebound bubble, prompting further investigation (Fig. 7D). The shadowgraph images of maximum bubble radius showed that μCBs generated near a prior damage site shifted laterally towards the damaged region relative to the location of laser focus (Fig. 7E). This displacement caused misalignment of the probe beam relative to the center of the μCB, resulting in an underestimation of the true μCB oscillation time and thereby resulting in a misleading increase in G_{HSR}. The magnitude of this displacement increased with decreasing distance from the damage site (Fig. 7F). Beyond a spacing of $\sim 2.5R_{max}$, the measured G_{HSR} matched baseline values established by the first μCB in each pair, indicating that the effects of μCB-induced

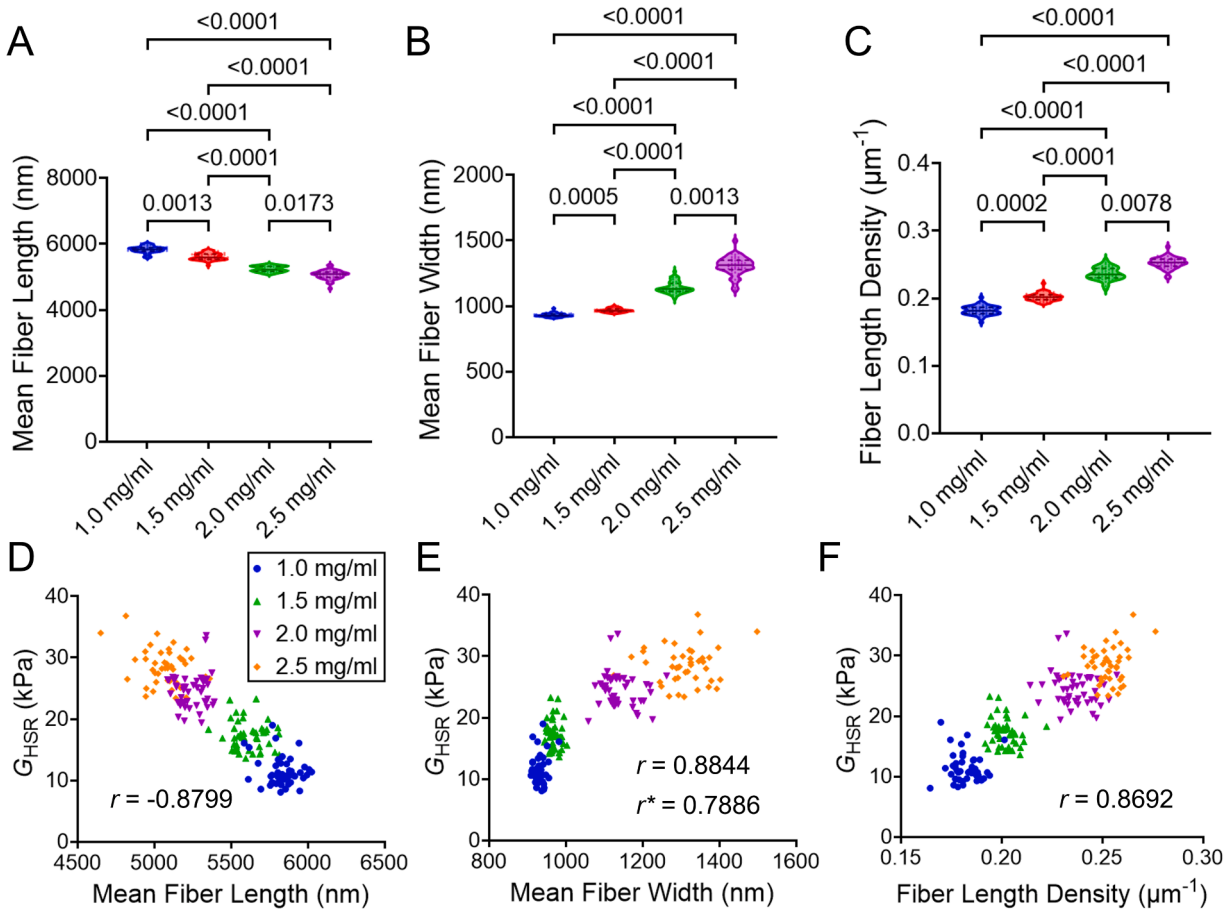


Fig. 6. Quantitative analysis of collagen fiber architecture metrics and their relationship to T1C concentration and shear modulus. (A-C) Effect of T1C concentration on structural parameters measured using GTFiber from reflection confocal microscopy images. (A) Mean fiber length decreases with increasing T1C concentration (B) Mean fiber width increases with increasing T1C concentration. (C) Fiber length density increases with increasing T1C concentration. Statistical comparisons were performed using the Kruskal-Wallis test with Dunn's multiple comparisons. (D-F) Correlation between shear modulus G_{HSR} and fiber structural parameters across all collagen concentrations. (D) Inverse correlation between G_{HSR} and mean fiber length ($r = -0.8799$, $p < 0.0001$). (E) Positive correlation between G_{HSR} and mean fiber width ($r = 0.8844$, $p < 0.0001$). r^* denotes the Spearman correlation coefficient excluding the 1.0 mg/mL group ($r = 0.7886$, $p < 0.0001$). (F) Positive correlation between G_{HSR} and fiber length density ($r = 0.8692$, $p < 0.0001$). r values represent the Spearman correlation coefficient. Data represent $n = 48$ measurements per condition across 3 independent hydrogel samples.

damage are spatially confined (Fig. 7C,F). We can therefore define the effective spatial resolution of sLCR as equivalent to roughly $2.5R_{max}$. To ensure that each μCB was generated in a region undisturbed by a previous μCB, all sLCR experiments were conducted with a minimum spacing of 318 μm.

4. Discussion

We introduce scanning Laser Cavitation Rheology (sLCR) as an accessible, non-contact method for spatially mapping the shear modulus G_{HSR} of soft materials at high strain rates. sLCR measurements showed an increase in G_{HSR} with T1C concentration (Fig. 4C), consistent with trends established by parallel-plate rheometry [34]. However, the high strain rate shear moduli measured by sLCR (~10–30 kPa) were approximately three orders of magnitude greater than quasi-static bulk values (Supplementary Fig. S3) [40]. This discrepancy in modulus is attributable to two factors. First, local mechanics in fibrillar networks can deviate from bulk properties by one to two orders of magnitude [41–43]. Second, μCB-induced deformations occur at rates ($> 10^4$ s^{-1}) exceeding the stress relaxation time of collagen fibers (seconds to hours), resulting in a strain stiffening effect [44,45]. Moreover, our findings are also in general agreement with our group's previous report of a laser cavitation-based rheology technique to measure the elastic response of fibrin and poly(ethylene glycol) diacrylate (PEGDA) hydrogels [25] where similar increases in the shear moduli at high strain rates were measured.

Notably, we employed a computationally lean, modified Rayleigh-Plesset (RP)-based bubble dynamics model for viscoelastic materials using a Neo-Hookean elasticity relationship for nonlinear material deformation [25,29]. Our choice of model aligns with our focus on spatially resolved mapping of biomaterial systems, where robust measurement and high throughput are prioritized. This approach assumes material isotropy and negligible time-dependent relaxation over the short timescale (~ 20 μs) of the first μCB oscillation. Prior work supports an elasticity-dominated response under these conditions, as semiflexible biopolymer networks behave predominantly elastically under large, rapid deformations [46], and viscous effects contributes minimally to the first oscillation μCB dynamics relative to elasticity [24]. While more advanced compressible material formulations (e.g. Keller-Miksis, Gilmore) are expected to better represent rebound dynamics and shock emission, recent analyses indicate that the first oscillation observables used in our method are only weakly sensitive to the choice of model [33,36,47]. Alternate constitutive relations (e.g. hyperelastic Fung) can capture additional behaviors such as viscous damping and nonlinear strain stiffening [24,48,49], but require fitting to more data points in order to retrieve additional parameters (e.g. strain stiffening coefficient α or viscosity μ). These parameters cannot be reliably determined using bubble oscillation time alone. Certainly, more sophisticated and

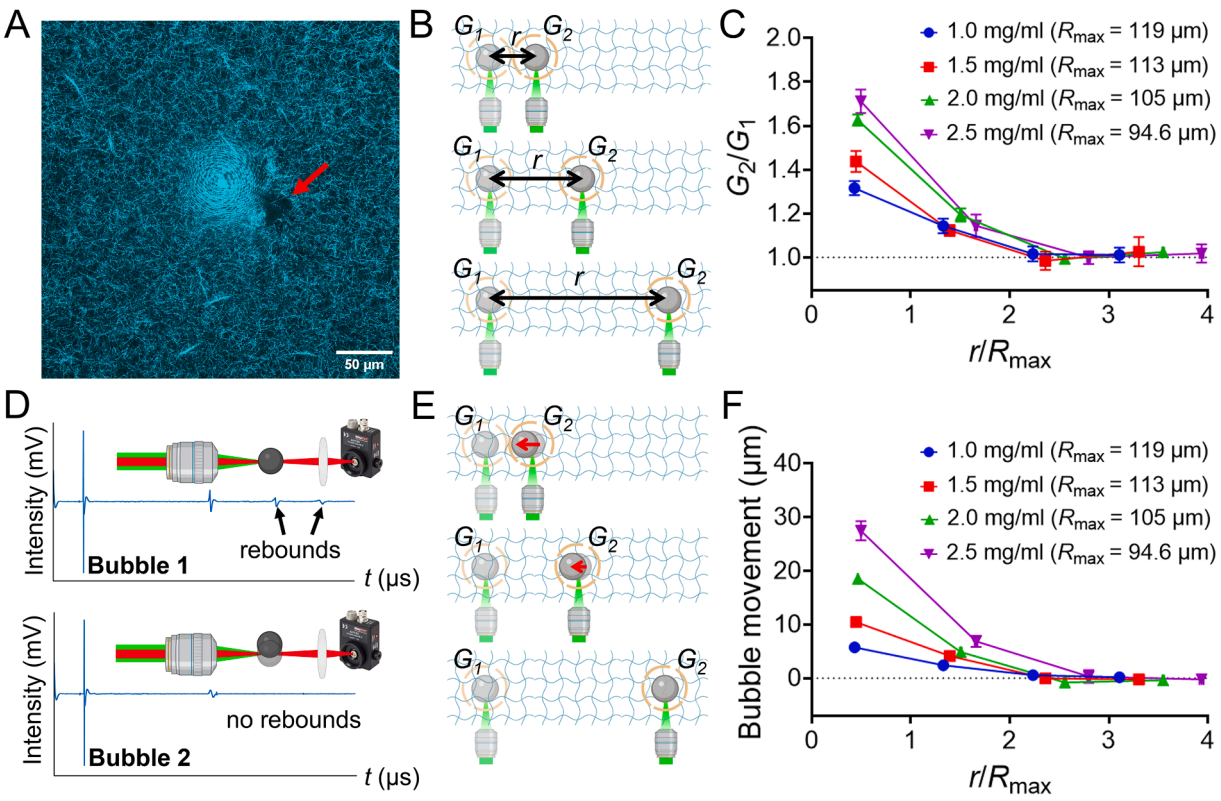


Fig. 7. μCB-induced matrix damage limits spatial resolution of sLCR. (A) Representative reflection confocal image showing the damage caused by a μCB (red arrow). (B) Schematic of the μCB pair experiment used to assess spatial resolution. Two sequential μCBs are generated at increasing distances r and the resulting shear moduli G_1 and G_2 are compared. (C) Ratio of moduli G_2/G_1 as a function of normalized μCB spacing r/R_{max}, showing an apparent elevated stiffness when bubble 2 was generated at locations within 2.5 R_{max} of bubble 1. Data are plotted as mean ± SEM. (D) Probe beam photodiode signals showing characteristic rebound oscillations for bubble 1 (top), and their absence in bubble 2 (bottom), consistent with misalignment of bubble 2 relative to the probe beam. (E) Schematic of μCB displacement, indicated by red arrows, toward the damaged region when μCB pairs are generated with lower center-to-center spacing. (F) Measured displacement of bubble 2 towards the damage zone of bubble 1 as a function of normalized spacing, showing persistent boundary effects up to ~2.5 R_{max}. Data are plotted as mean ± SEM.

potentially more accurate models can be utilized, and we see this as a natural next step in future implementations of sLCR that incorporate additional observables, such as a complete interferometric measurement of the μCB dynamics [50], for a more comprehensive characterization of high strain rate mechanics.

Because our current sLCR implementation utilizes single measurements of R_{max} and T, rather than a full $R(t)$ trace, we do not reconstruct the complete temporal evolution of strain and strain rate during μCB loading. Instead, we can report estimates of the loading regime based on the measured R_{max} and T values. The engineering strain produced at maximum bubble expansion (R_{max} ~ 100–125 μm) can be approximated as $\varepsilon \sim R_{max}/R_0 - 1$. Moreover, this strain occurs over the timescale of half the bubble oscillation time (T ~ 15–20 μs), corresponding to approximate average strain rates of $\dot{\varepsilon} \sim 2\varepsilon/T$. This provides maximum strain and average strain rate estimates of ~1.5 (150 %) and ~10^5 s^{-1}, respectively, consistent with prior μCB analyses using continuum frameworks [25,51]. This high strain, high-rate loading regime is comparable to loads experienced by tissue during several clinical procedures including lithotripsy [19,52], histotripsy [53], and laser eye surgery [17].

To investigate the structural basis of concentration-dependent stiffening, we analyzed co-registered reflection confocal images of the collagen fiber structure. At lower concentrations (1.0 and 1.5 mg/mL), fiber width measurements clustered toward the lower bound of the measurement range (Fig. 6E). While none of the measured fiber widths fell below the diffraction limit (~238 nm), they began to approach the minimum feature size that can be reliably resolved by reflection confocal microscopy. Consequently, the variations in fiber width may be underestimated in the 1.0 and 1.5 mg/mL gels. Importantly, reflection confocal imaging preferentially detects fibers that are oriented perpendicular to the optical axis, while fibers oriented parallel to the optical axis are underrepresented. Moreover, although G_{HSR} correlates with fiber length, width, and length density when pooling data across concentrations, the absence of significant correlations within a single concentration suggests that G_{HSR} is not governed by any single metric quantified here (Fig. 6D-F). This result is consistent with prior studies combining second harmonic generation (SHG) imaging and local mechanical measurements, where stiffness was not uniquely predicted by SHG-derived collagen fiber metrics only but also influenced by parameters such as nanoscale fibril organization and collagen crosslinking [54–56]. Future work will further investigate the relationship between G_{HSR} and fiber properties by expanding the structural descriptors available from co-registered imaging, including 3D confocal reconstructions of the collagen network [57], fluorescent labeling collagen to enable orientation-independent fiber detection [58], and deep learning-based segmentation strategies to maximize the information available from label-free imaging approaches [59].

Our results demonstrate that the spatial resolution of sLCR is constrained by μCB-induced matrix damage. Specifically, when repeated sLCR measurements are made at locations within approximately 2.5× the maximum μCB radius, the local weakening of the hydrogel leads to lateral displacement of subsequent μCBs formed proximal to the initial bubble. This results in probe beam misalignment and an erroneously shortened measurement of μCB oscillation time, resulting in an apparent increase in shear modulus. The spatial extent of such boundary effects that cause lateral bubble motion is consistent with similar observations in fluid cavitation [60,61]. However, to the best of our knowledge, this phenomenon has not been reported for cavities within soft biomaterials. To avoid this phenomenon, all measurements were conducted with

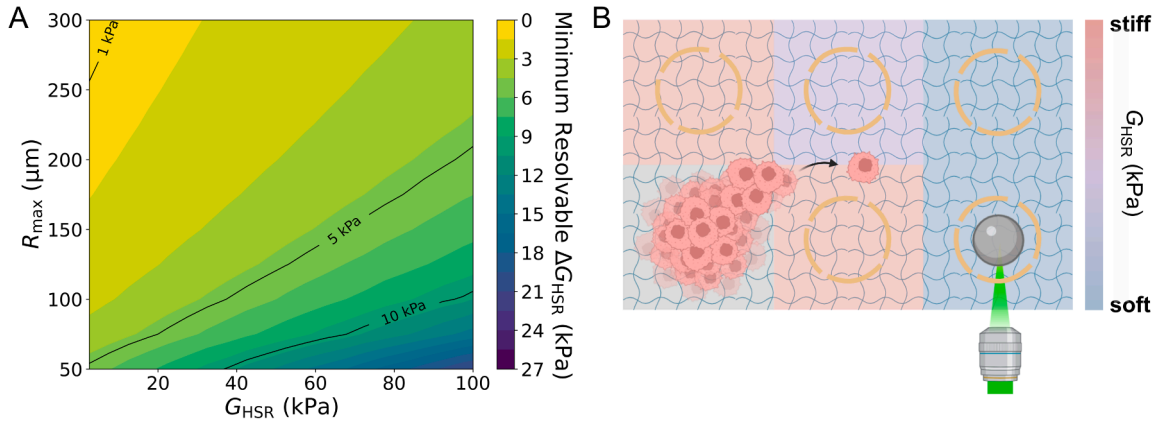


Fig. 8. Sensitivity and potential biological application of sLCR. (A) Contour map showing the minimum resolvable change in shear modulus ΔG_{HSR} as a function of μCB radius and material stiffness. Values are based on forward simulations of our bubble dynamics model, incorporating experimental noise from 50 μCB generated in DI water. Contour lines of ΔG_{HSR} = 1, 5, and 10 kPa are shown. (B) Illustration of the biological application of sLCR to spatially map the mesoscale mechanical properties of the heterogeneous tumor-stroma interface in a 3D matrix.

spacing greater than 2.5× the maximum μCB radius.

Although the spatial resolution of sLCR could be improved by reducing the bubble size, this comes at the cost of reduced sensitivity to high strain rate shear modulus G_{HSR} (Fig. 8A). We quantified the sensitivity of sLCR by calculating the minimum resolvable change in shear modulus (ΔG_{HSR}) with 95 % confidence using the standard limit of detection (LOD) formula [62]:

$$\Delta G_{HSR} = \frac{k\sigma_T}{(dT/dG_{HSR})} \quad (5)$$

where σ_T is the experimental noise level, measured as the standard deviation of the oscillation time measured from generating 50 μCBs in deionized (DI) water, k is the confidence multiplier (k = 2 for 95 % confidence), and (dT/dG_{HSR}) is the change in oscillation time for a given change in G_{HSR} as determined from forward simulations of the bubble dynamics model (Supplementary Fig. S11). The resulting ΔG_{HSR} values, plotted as a function of G_{HSR} and maximum bubble radius for 95 % confidence (Fig. 8A), provide a practical guide for selecting a bubble size based on the expected material stiffness and desired sensitivity. The sensitivity with alternate confidence levels is shown in Supplementary Fig. S12. Sensitivity to G_{HSR} improves with larger R_{max} and lower G_{HSR} values. Therefore, the use of larger μCBs is better suited for characterizing stiffer materials. Conversely, the use of smaller μCBs provides improved spatial resolution at the expense of reduced sensitivity to G_{HSR} and is thus best suited for probing softer materials where the sensitivity is inherently greater. In practice, implementing adaptive μCB sizing to optimize sensitivity requires adjustment of the camera trigger delay and exposure time to reliably capture R_{max} via shadowgraphy (Supplementary Fig. S2). Under the conditions explored in this study (G_{HSR} < 50 kPa; R_{max} > 100 μm), sLCR achieved a predicted sensitivity of approximately 3 kPa. The apparent intra-gel variability observed in the spatial maps of G_{HSR} (Fig. 5A) was comparable to this detection limit, indicating that variations smaller than ~3 kPa are not resolvable in the current operating regime. Given the ~300 μm effective spatial resolution, each sLCR measurement averages the material properties over multiple pores [34]. Importantly, sLCR does not require the assumption of uniform optical absorption in a heterogeneous sample. By simultaneously measuring both R_{max} and T at each measurement site, we mitigate bias from spatial variations in absorption or scattering.

Fig. 8B illustrates the biological significance of sLCR's sensitivity, as the technique is well suited to resolve mesoscale mechanical changes that accompany tissue remodeling. For example, several studies have shown that the invasive front of human breast cancers is stiffer by ~2–20 kPa relative to adjacent normal stroma over distances of 100–500 μm [63–65]. Similar mesoscale stiffening occurs in fibrosis, where fibrotic regions of mouse lungs increase in stiffness by tens of kilopascals compared to adjacent normal tissue [66]. Our implementation of sLCR using ~100 μm radius μCBs provides a detection limit of ~3 kPa and an effective spatial resolution of ~300 μm, which is well matched to interrogate such variations in stiffness. Future implementations of sLCR with complementary biological assays (e.g. matrix remodeling assays) will expand its utility for probing dynamic mechanical changes across various disease contexts.

5. Conclusion

This study introduces scanning Laser Cavitation Rheology (sLCR) as a non-contact technique for high strain rate (> 10^4 s^{-1}) mechanical mapping of soft materials at the mesoscopic scale. sLCR has utility in characterizing both the material response to rapid loading events (e.g. blast injury, lithotripsy, laser surgery) and the slower remodeling processes in which T1C is deposited such as in cancer, fibrosis, and wound healing. We demonstrate the utility of sLCR in T1C hydrogels by capturing the expected stiffening with increasing collagen concentration, quantifying the microstructural basis of concentration-dependent stiffening with co-registered reflection confocal microscopy, and establishing a framework to quantify the sensitivity and spatial resolution limits of the technique. Together, these results define the operating parameters for applying sLCR across a wide range of soft material systems. By bridging the gap between bulk rheometry and microrheology, sLCR provides a unique platform to interrogate the mechanics of soft biomaterials under high strain rate loading and serves as a broadly applicable tool for probing dynamic mechanical changes in biologically relevant contexts.

CRediT authorship contribution statement

Rahul Sreedasyam: Writing – review & editing, Writing – original draft, Visualization, Validation, Software, Methodology, Investigation, Formal analysis, Data curation. **Ethan C. Vu:** Visualization, Software. **Shreya Thota:** Data curation. **Elliot L. Botvinick:** Writing – review & editing, Supervision, Resources, Project administration, Methodology, Funding acquisition, Conceptualization. **Vasan Venugopalan:** Writing – review & editing, Supervision, Resources, Project administration, Methodology, Funding acquisition, Conceptualization.

Declaration of competing interest

The authors declare that they have no known competing financial

interests or personal relationships that could have appeared to influence the work reported in this paper.

Acknowledgments

This work was supported by the National Institutes of Health (R01 GM129426).

Supplementary materials

Supplementary material associated with this article can be found, in the online version, at doi:10.1016/j.actbio.2026.03.024.

References

[1] S.R. Peyton, A.J. Putnam, Extracellular matrix rigidity governs smooth muscle cell motility in a biphasic fashion, J. Cell Physiol. 204 (1) (2005) 198–209.
[2] A.J. Engler, S. Sen, H.L. Sweeney, D.E. Discher, Matrix elasticity directs stem cell lineage specification, Cell 126 (4) (2006) 677–689.
[3] D.T. Butcher, T. Alliston, V.M. Weaver, A tense situation: forcing tumour progression, Nat. Rev. Cancer 9 (2) (2009) 108–122.
[4] O. Chaudhuri, J. Cooper-White, P.A. Janmey, D.J. Mooney, V.B. Shenoy, Effects of extracellular matrix viscoelasticity on cellular behaviour, Nature 584 (7822) (2020) 535–546.
[5] A. Isomursu, K.Y. Park, J. Hou, B. Cheng, M. Mathieu, G.A. Shamsan, B. Fuller, J. Kasim, M.M. Mahmoodi, T.J. Lu, G.M. Genin, F. Xu, M. Lin, M.D. Distefano, J. Ivaska, D.J. Odde, Directed cell migration towards softer environments, Nat. Mater. 21 (9) (2022) 1081–1090.
[6] S.P. Zustiak, J.B. Leach, Hydrolytically degradable poly(ethylene glycol) hydrogel scaffolds with tunable degradation and mechanical properties, Biomacromolecules 11 (5) (2010) 1348–1357.
[7] A. Banerjee, M. Arha, S. Choudhary, R.S. Ashton, S.R. Bhatia, D.V. Schaffer, R. S. Kane, The influence of hydrogel modulus on the proliferation and differentiation of encapsulated neural stem cells, Biomaterials 30 (27) (2009) 4695–4699.
[8] A. Jagieło, U. Castillo, E. Botvinick, Cell mediated remodeling of stiffness matched collagen and fibrin scaffolds, Sci. Rep. 12 (1) (2022) 11736.
[9] B.J. DuChez, A.D. Doyle, E.K. Dimitriadis, K.M. Yamada, Durotaxis by Human cancer cells, Biophys. J. 116 (4) (2019) 670–683.
[10] B.F. Kennedy, R.A. McLaughlin, K.M. Kennedy, L. Chin, A. Curatolo, A. Tien, B. Latham, C.M. Saunders, D.D. Sampson, Optical coherence micro-elastography: mechanical-contrast imaging of tissue microstructure, Biomed. Opt. Express. 5 (2014) 2113–2124.
[11] Z. Hajjarian, H.T. Nia, S. Ahn, A.J. Grodzinsky, R.K. Jain, S.K. Nadkarni, Laser Speckle rheology for evaluating the viscoelastic properties of hydrogel scaffolds, Sci. Rep. 6 (2016) 37949.
[12] M. Keating, A. Kurup, M. Alvarez-Elizondo, A.J. Levine, E. Botvinick, Spatial distributions of pericellular stiffness in natural extracellular matrices are dependent on cell-mediated proteolysis and contractility, Acta Biomater. 57 (2017) 304–312.
[13] R.M. Robertson-Anderson, Optical tweezers microrheology: from the basics to advanced techniques and applications, ACS. Macro Lett. 7 (8) (2018) 968–975.
[14] C.A. Jones, M. Cibula, J. Feng, E.A. Krnacik, D.H. McIntyre, H. Levine, B. Sun, Micromechanics of cellularized biopolymer networks, in: Proceedings of the National Academy of Sciences of the United States of America 112, 2015, pp. E5117–E5122.
[15] J.B. Estrada, H.C. Cramer, M.T. Scimone, S. Buyukozturk, C. Franck, Neural cell injury pathology due to high-rate mechanical loading, Brain Multiphys. 2 (2021) 100034.
[16] E. Bar-Kochba, M.T. Scimone, J.B. Estrada, C. Franck, Strain and rate-dependent neuronal injury in a 3D in vitro compression model of traumatic brain injury, Sci. Rep. 6 (2016) 30550.
[17] A. Vogel, V. Venugopalan, Mechanisms of pulsed laser ablation of biological tissues, Chem. Rev. 103 (2) (2003) 577–644.
[18] A. Vogel, V. Venugopalan, Pulsed laser ablation of soft biological tissues, in: A. Welch, M. van Gemert (Eds.), Optical-Thermal Response of Laser-Irradiated Tissue, Springer, Dordrecht, 2010.
[19] D. Howard, B. Sturtevant, In vitro study of the mechanical effects of shock-wave lithotripsy, Ultrasound. Med. Biol. 23 (7) (1997) 1107–1122.
[20] W. Chen, B. Song, Split Hopkinson (Kolsky) Bar: Design, Testing, and Applications, Springer, New York, 2011.
[21] C.E. Dougan, H. Fu, A.J. Crosby, S.R. Peyton, Needle-induced cavitation: a method to probe the local mechanics of brain tissue, J. Mech. Behav. Biomed. Mater. 160 (2024) 106698.
[22] K.M. Evans, C.L. Soles, E.P. Chan, Studying the high-rate deformation of soft materials via laser-induced membrane expansion, Soft. Matter. 19 (2) (2023) 276–281.
[23] J. Mondal, R. Lakkaraju, P. Ghosh, M. Ashokkumar, Acoustic cavitation-induced shear: a mini-review, Biophys. Rev. 13 (6) (2021) 1229–1243.
[24] J.B. Estrada, C. Barajas, D.L. Henann, E. Johnsen, C. Franck, High strain-rate soft material characterization via inertial cavitation, J. Mech. Phys. Solids. 112 (2018) 291–317.
[25] J.C. Luo, H. Ching, B.G. Wilson, A. Mohraz, E.L. Botvinick, V. Venugopalan, Laser cavitation rheology for measurement of elastic moduli and failure strain within hydrogels, Sci. Rep. 10 (2020) 13144.
[26] S. Tiwari, A. Kazemi-Moridani, Y. Zheng, C.W. Barney, K.R. McLeod, C.E. Dougan, A.J. Crosby, G.N. Tew, S.R. Peyton, S. Cai, J.H. Lee, Seeded laser-induced cavitation for studying high-strain-rate irreversible deformation of soft materials, Soft. Matter. 16 (39) (2020) 9006–9013.
[27] S.R. Caliari, J.A. Burdick, A practical guide to hydrogels for cell culture, Nat. Methods 13 (5) (2016) 405–414.
[28] M.D. Shoulders, R.T. Raines, Collagen structure and stability, Annu. Rev. Biochem. 78 (1) (2009) 929–958.
[29] R. Gaudron, M.T. Warnez, E. Johnsen, Bubble dynamics in a viscoelastic medium with nonlinear elasticity, J. Fluid. Mech. 766 (2015) 54–75.
[30] P.H. Brown, A. Balbo, H. Zhao, C. Ebel, P. Schuck, Density contrast sedimentation velocity for the determination of protein partial-specific volumes, PLoS. One 6 (10) (2011) e26221.
[31] C. Li, J. Ma, Q. Fan, Y. Tao, G. Li, Dynamic light scattering (DLS)-based immunoassay for ultra-sensitive detection of tumor marker protein, Chem. Commun. 52 (50) (2016) 7850–7853.
[32] A.T. Palasz, J. Thundathil, R.E. Verrall, R.J. Mapletoft, The effect of macromolecular supplementation on the surface tension of TCM-199 and the utilization of growth factors by bovine oocytes and embryos in culture, Anim. Reprod. Sci. 58 (3–4) (2000) 229–240.
[33] X.X. Liang, N. Linz, S. Freidank, G. Paltauf, A. Vogel, Comprehensive analysis of spherical bubble oscillations and shock wave emission in laser-induced cavitation, J. Fluid. Mech. 940 (2022) A5.
[34] Y.L. Yang, L.M. Leone, L.J. Kaufman, Elastic moduli of collagen gels can be predicted from two-dimensional confocal microscopy, Biophys. J. 97 (7) (2009) 2051–2060.
[35] C.E. Brennen, Cavitation and Bubble Dynamics, Cambridge University Press, 2014.
[36] J. Yang, A. McGhee, G. Radtke, M. Rodriguez, C. Franck, Estimating viscoelastic, soft material properties using a modified Rayleigh cavitation bubble collapse time, Phys. Fluids 36 (1) (2024).
[37] Z. Zhu, S. Remillard, B.A. Abeid, D. Frolkin, S.H. Bryngelson, J. Yang, J.B. Estrada, Parsimonious inertial cavitation rheometry via bubble collapse time, Soft Matter 21 (34) (2025) 6717–6734.
[38] I. Usov, R. Mezzenga, FiberApp: an open-source software for tracking and analyzing polymers, filaments, biomacromolecules, and fibrous objects, Macromolecules 48 (5) (2015) 1269–1280.
[39] Imperssonator, Public Repository for GTFiber version 2, GitHub (2025). Accessed November 2, https://github.com/Imperssonator/GTFiber2.
[40] R.C. Arevalo, J.S. Urbach, D.L. Blair, Size-dependent rheology of type-I collagen networks, Biophys. J. 99 (8) (2010) L65–L67.
[41] B. Sun, The mechanics of fibrillar collagen extracellular matrix, Cell Rep. Phys. Sci. 2 (8) (2021).
[42] M. Shayegan, N.R. Forde, Microrheological characterization of collagen systems: from molecular solutions to fibrillar gels, PLoS. One 8 (8) (2013) e70590.
[43] M.A. Kotlarchyk, S.G. Shreim, M.B. Alvarez-Elizondo, L.C. Estrada, R. Singh, L. Valdevit, E. Kniazeva, E. Gratton, A.J. Putnam, E.L. Botvinick, Concentration independent modulation of local micromechanics in a fibrin gel, PLoS. One 6 (5) (2011) e20201.
[44] S.E. Szczesny, D.M. Elliott, Interfibrillar shear stress is the loading mechanism of collagen fibrils in tendon, Acta Biomater. 10 (6) (2014) 2582–2590.
[45] A. Gautieri, S. Vesentini, A. Redaelli, M.J. Buehler, Viscoelastic properties of model segments of collagen molecules, Matrix. Biol. 31 (2) (2012) 141–149.
[46] C.P. Broedersz, C. Storm, F.C. MacKintosh, Nonlinear elasticity of composite networks of stiff biopolymers with flexible linkers, Phys. Rev. Lett. 101 (11) (2008) 118103.
[47] A. Tzoumaka, J. Yang, S. Buyukozturk, C. Franck, D.L. Henann, Modeling high strain-rate microcavitation in soft materials: the role of material behavior in bubble dynamics, Soft. Matter. 19 (21) (2023) 3895–3909.
[48] Y.C. Fung, Biomechanics: Mechanical Properties of Living Tissues, Springer Science & Business Media, 2013.
[49] J. Yang, C. Franck, Strain stiffening effects of soft viscoelastic materials in inertial microcavitation. In dynamic behavior of materials, in: Proceedings of the 2019 Annual Conference on Experimental and Applied Mechanics 1, Springer International Publishing, Cham, 2019, pp. 175–179.
[50] B.G. Wilson, Z. Fan, R. Sreedasyam, E.L. Botvinick, V. Venugopalan, Single-shot interferometric measurement of cavitation bubble dynamics, Opt. Lett. 46 (6) (2021) 1409–1412.
[51] R. Sreedasyam, B.G. Wilson, P.R. Ferrandez, E.L. Botvinick, V. Venugopalan, An optical system for cellular mechanostimulation in 3D hydrogels, Acta Biomater. 189 (2024) 439–448.
[52] R.O. Cleveland, O.A. Sapozhnikov, Modeling elastic wave propagation in kidney stones with application to shock wave lithotripsy, J. Acoust. Soc. Am. 118 (4) (2005) 2667–2676.
[53] L. Mancia, E. Vlaisavljevich, N. Yousefi, M. Rodriguez, T.J. Ziemlewicz, F.T. Lee, D. Henann, C. Franck, E. Johnsen, Modeling tissue-selective cavitation damage, Phys. Med. Biol. 64 (22) (2019) 225001.
[54] M.G. Jones, O.G. Andriotis, J.J. Roberts, K. Lunn, V.J. Tear, L. Cao, K. Ask, D. E. Smart, A. Bonfanti, P. Johnson, P.J. …Thurner, D.E. Davies, Nanoscale dysregulation of collagen structure-function disrupts mechano-homeostasis and mediates pulmonary fibrosis, Elife 7 (2018) e36354.
[55] C.A. Couture, S. Bancelin, J. Van der Kolk, K. Popov, M. Rivard, K. Légaré, F. Légaré, The impact of collagen fibril polarity on second harmonic generation microscopy, Biophys. J. 109 (12) (2015) 2501–2510.

[56] R.M. Williams, W.R. Zipfel, W.W. Webb, Interpreting second-harmonic generation images of collagen I fibrils, Biophys. J. 88 (2) (2005) 1377–1386.
[57] V.V. Artym, K. Matsumoto, Imaging cells in three-dimensional collagen matrix, Curr. Protoc. Cell Biol. 48 (1) (2010) 10–18.
[58] A.D. Doyle, Fluorescent labeling of rat-tail collagen for 3D fluorescence imaging, Bio Protoc. 8 (13) (2018) e2919, e2919.
[59] S. Eldeen, A.F.G. Ramirez, B. Keresteci, P.D. Chang, E.L. Botvinick, Label-free prediction of fluorescently labeled fibrin networks, Biomater. Res. 29 (2025) 0211.
[60] J.R. Blake, D.C. Gibson, Cavitation bubbles near boundaries, Annu Rev. Fluid. Mech. 19 (1) (1987) 99–123.
[61] E.A. Brujan, G.S. Keen, A. Vogel, J.R. Blake, The final stage of the collapse of a cavitation bubble close to a rigid boundary, Phys. Fluids 14 (1) (2002) 85–92.
[62] L.A. Currie, Limits for qualitative detection and quantitative determination. application to radiochemistry, Anal. Chem. 40 (3) (1968) 586–593.
[63] I. Acerbi, L. Cassereau, I. Dean, Q. Shi, A. Au, C. Park, Y.Y. Chen, J. Liphardt, E. S. Hwang, V.M. Weaver, Human breast cancer invasion and aggression correlates with ECM stiffening and immune cell infiltration, Integr Biol 7 (10) (2015) 1120–1134.
[64] K.R. Levental, H. Yu, L. Kass, J.N. Lakins, M. Egeblad, J.T. Erler, S.F.T. Fong, K. Csiszar, A. Giaccia, W. Weninger, M. Yamauchi, D.L. Gasser, V.M. Weaver, Matrix crosslinking forces tumor progression by enhancing integrin signaling, Cell 139 (5) (2009) 891–906.
[65] M.J. Paszek, N. Zahir, K.R. Johnson, J.N. Lakins, G.I. Rozenberg, A. Gefen, C. A. Reinhart-King, S.S. Margulies, M. Dembo, D. Boettiger, D.A. Hammer, V. M. Weaver, Tensional homeostasis and the malignant phenotype, Cancer Cell 8 (3) (2005) 241–254.
[66] E. Melo, N. Cárdenes, E. Garreta, T. Luque, M. Rojas, D. Navajas, R. Farré, Inhomogeneity of local stiffness in the extracellular matrix scaffold of fibrotic mouse lungs, J. Mech. Behav. Biomed. Mater. 37 (2014) 186–195.